



Tentative Evidence for Water Vapor in the Atmosphere of the Neptune-sized Exoplanet HD 106315c

Laura Kreidberg^{1,2} , Paul Mollière¹ , Ian J. M. Crossfield³, Daniel P. Thorngren⁴ , Yui Kawashima⁵ , Caroline V. Morley⁶ , Björn Benneke⁴ , Thomas Mikal-Evans⁷ , David Berardo⁷ , Molly R. Kosiarek^{8,26} , Varoujan Gorjian⁹ , David R. Ciardi¹⁰ , Jessie L. Christiansen¹⁰ , Diana Dragomir¹¹ , Courtney D. Dressing¹² , Jonathan J. Fortney¹³ , Benjamin J. Fulton¹⁴ , Thomas P. Greene¹⁵ , Kevin K. Hardegree-Ullman¹⁰ , Andrew W. Howard¹⁶ , Steve B. Howell¹⁷ , Howard Isaacson^{12,18} , Jessica E. Krick¹⁹ , John H. Livingston²⁰ , Joshua D. Lothringer²¹ , Farisa Y. Morales²² , Erik A. Petigura²³ , Joseph E. Rodriguez² , Joshua E. Schlieder²⁴ , and Lauren M. Weiss²⁵

¹Max-Planck-Institut für Astronomie, Königstuhl 17, D-69117 Heidelberg, Germany; kreidberg@mpia.de

²Center for Astrophysics | Harvard & Smithsonian, 60 Garden Street, Cambridge, MA, 02138, USA

³The University of Kansas, Department of Physics and Astronomy, Malott Room 1082, 1251 Wescoe Hall Drive, Lawrence, KS, 66045, USA

⁴Institute for Research on Exoplanets, Université de Montréal, Montréal, Quebec, H3T 1J4, Canada

⁵Cluster for Pioneering Research, RIKEN, 2-1 Hirosawa, Wako, Saitama 351-0198, Japan

⁶Department of Astronomy, University of Texas at Austin, Austin, TX 78712, USA

⁷Kavli Institute for Astrophysics and Space Research, Massachusetts Institute of Technology, 77 Massachusetts Avenue, 37-241, Cambridge, MA 02139, USA

⁸Department of Astronomy and Astrophysics, University of California, Santa Cruz, CA 95064, USA

⁹MS 169-506, Jet Propulsion Laboratory, California Institute of Technology, 4800 Oak Grove Drive, Pasadena, CA 91109, USA

¹⁰Caltech/IPAC-NExScI, M/S 100-22, 770 S Wilson Avenue, Pasadena, CA 91106 USA

¹¹Department of Physics and Astronomy, University of New Mexico, 1919 Lomas Boulevard NE, Albuquerque, NM 87131, USA

¹²Department of Astronomy, 501 Campbell Hall, University of California at Berkeley, Berkeley, CA 94720, USA

¹³Department of Astronomy & Astrophysics, University of California, Santa Cruz, CA 95064, USA

¹⁴NASA Exoplanet Science Institute/Caltech-IPAC, Pasadena, CA 91125, USA

¹⁵Space Science and Astrobiology Division, NASA Ames Research Center, MS 245-6, Moffett Field, CA 94035, USA

¹⁶California Institute of Technology, Pasadena, CA 91125, USA

¹⁷NASA Ames Research Center, Moffett Field, CA 94035, USA

¹⁸Centre for Astrophysics, University of Southern Queensland, Toowoomba, QLD, Australia

¹⁹Caltech/IPAC, M/S 330-6, 1200 E. California Boulevard, Pasadena, CA 91125 USA

²⁰Department of Astronomy, University of Tokyo, 7-3-1 Hongo, Bunkyo-ku, Tokyo 113-0033, Japan

²¹Department of Physics and Astronomy, Johns Hopkins University, Baltimore, MD 21218, USA

²²MS 169-214, Jet Propulsion Laboratory, California Institute of Technology, 4800 Oak Grove Drive, Pasadena, CA 91109, USA

²³Department of Physics & Astronomy, University of California Los Angeles, Los Angeles, CA 90095, USA

²⁴Exoplanets and Stellar Astrophysics Laboratory, Code 667, NASA Goddard Space Flight Center, Greenbelt, MD 20771, USA

²⁵Institute for Astronomy, University of Hawai'i, 2680 Woodlawn Drive, Honolulu, HI 96822, USA

Received 2020 June 12; revised 2022 May 29; accepted 2022 July 30; published 2022 September 6

Abstract

We present a transmission spectrum for the Neptune-sized exoplanet HD 106315c from optical to infrared wavelengths based on transit observations from the Hubble Space Telescope/Wide Field Camera 3, K2, and Spitzer. The spectrum shows tentative evidence for a water absorption feature in the 1.1–1.7 μm wavelength range with a small amplitude of 30 ppm (corresponding to just 0.8 ± 0.04 atmospheric scale heights). Based on an atmospheric retrieval analysis, the presence of water vapor is tentatively favored with a Bayes factor of 1.7–2.6 (depending on prior assumptions). The spectrum is most consistent with either an enhanced metallicity or high-altitude condensates, or both. Cloud-free solar composition atmospheres are ruled out at $>5\sigma$ confidence. We compare the spectrum to grids of cloudy and hazy forward models and find that the spectrum is fit well by models with moderate cloud lofting or haze formation efficiency over a wide range of metallicities (1–100 \times solar). We combine the constraints on the envelope composition with an interior structure model and estimate that the core mass fraction is $\gtrsim 0.3$. With a bulk composition reminiscent of that of Neptune and an orbital distance of 0.15 au, HD 106315c hints that planets may form out of broadly similar material and arrive at vastly different orbits later in their evolution.

Unified Astronomy Thesaurus concepts: [Exoplanet atmospheres \(487\)](#); [Water vapor \(1791\)](#); [Hot Neptunes \(754\)](#); [Exoplanets \(498\)](#); [Atmospheric clouds \(2180\)](#)

1. Introduction

The origins of Uranus and Neptune remain mysterious. Based on current data, it is not known if they formed by core accretion or gravitational instability, whether they grew in their current locations or underwent migration, or how long it took them to form (Atreya et al. 2020, and references therein). One of the challenges in modeling these planets' origin is that their bulk composition is poorly constrained. Uranus and Neptune are so cold that many of the dominant carbon-, nitrogen-, and

²⁶ NSF Graduate Research Fellow



oxygen-bearing molecules have condensed out of the observable atmosphere, leaving only methane accessible by remote observation (Helled et al. 2020). There are calls for a space mission to explore one of the ice giants in situ and measure its atmospheric abundances directly with a probe; however, such a mission is over a decade away (Simon et al. 2020).

Meanwhile the search for extrasolar planets has revealed an abundance of Neptune-sized worlds (e.g., Coughlin et al. 2016). Many of these have short orbital periods and correspondingly high equilibrium temperatures (up to 2000 K), meaning that major volatile species are expected to be in the gas phase in the observable part of the atmosphere (Moses et al. 2013). Atmosphere characterization of these hotter exo-Neptunes provides an opportunity to determine their chemical compositions, well in advance of in situ measurements of the solar system ice giants.

Precise near-infrared transmission spectra are available for fewer than a dozen exoplanets in the Neptune-mass range, $10\text{--}40 M_{\oplus}$ (Crossfield & Kreidberg 2017; Kreidberg et al. 2018b; Mansfield et al. 2018; Spake et al. 2018; Benneke et al. 2019a, 2019b; Chachan et al. 2019; Guo et al. 2020; Libby-Roberts et al. 2020). Planets of this size are expected to have modest H/He envelopes ($\gtrsim 1\%$ by mass), with a diversity of atmospheric metal enrichment (e.g., Fortney et al. 2013; Wolfgang & Lopez 2015). The transmission spectra measured to date have a wide range of properties that match the diversity expected from theoretical models. Some planets appear to have very high metallicity envelopes (e.g., the $\sim 1000\times$ solar composition inferred for GJ 436b; Morley et al. 2017). Others have lower metallicity, more akin to Jupiter’s $<10\times$ solar composition (HAT-P-26b; Wakeford et al. 2017). The planets also have a wide range of cloud and haze properties, from cloud-free to very high altitude condensates, which complicate the interpretation of the measured spectra (Kreidberg et al. 2014; Crossfield & Kreidberg 2017). To fully explore the diversity of the exo-Neptune population and identify cloud-free atmospheres, a larger sample size is needed, which is the goal of the ongoing large Hubble Space Telescope (HST) program GO 15333 (PIs I. Crossfield and L. Kreidberg). In total this program will obtain transmission spectra for five additional Neptune-sized exoplanets, including the subject of this work, HD 106315c.

First observed by the K2 mission (Crossfield et al. 2017; Rodriguez et al. 2017), HD 106315c has a radius of $4.379 \pm 0.086 R_{\oplus}$ and a mass of $12.0 \pm 3.8 M_{\oplus}$ (Kosiarek et al. 2021). The planet has a 21.06 day orbit around its F5-type host star, and an equilibrium temperature of 870 ± 20 K (assuming full heat redistribution and zero Bond albedo). Thanks to the bright host (H magnitude = 8.0), HD 106315c is one of the most accessible candidates for atmosphere characterization with transmission spectroscopy, with a Transmission Spectroscopy Metric equal to 119 (this metric is a proxy for the expected signal-to-noise ratio of the transmission spectrum; Kempton et al. 2018). Compared to other exo-Neptunes with precise spectra, HD 106315c has a longer period and a more massive host star (Crossfield & Kreidberg 2017). It is also part of a multiplanet system, with an interior $2.6 R_{\oplus}$ planet orbiting the star every 9.6 days.

2. Observations

We observed four transits of HD 106315c with the Wide Field Camera 3 (WFC3) instrument on HST as part of Program

GO 15333 (Co-PIs: I. Crossfield and L. Kreidberg). The dates of the observations were 2018 December 3, 2018 December 21–22, 2019 February 2, and 2019 November 21. There was also an observation on 2018 June 15 that failed due to lost guiding. Each transit observation consists of time-series exposures over six continuous HST orbits. The first exposure of each orbit was a direct image with the F126N filter. Subsequent exposures used the G141 grism, which covers the wavelength range from 1.1 to $1.7 \mu\text{m}$. The exposures used the SPARS25, NSAMP = 8 readout mode, which has a total integration time of 138.4 s. The observations used the spatial scanning mode, which spreads the light in the cross-dispersion direction during the exposure, enabling longer integration times before saturation (Deming et al. 2013). The scan rate was $0''.213 \text{ s}^{-1}$, yielding a total scan height of $31''$ (238 pixels). We observed 14 exposures per orbit, for an observing efficiency of 73%.

A single transit was also observed by the Spitzer Space Telescope (Fazio et al. 2004; Werner et al. 2004) with the IRAC2 $4.5 \mu\text{m}$ photometric channel on 2017 April 19–20 as part of Program 13052 (PI: M. Werner). The observations used the PCRS peak-up mode, which positions the target precisely on a pixel with minimal sensitivity variations.²⁷ The observation began with a 30 minute stare to allow the spacecraft to thermally settle, followed by 32,168 s (8.9 hr) of science data with an exposure time of 0.4 s. Two transits were also observed by K2 (previously described in Crossfield & Kreidberg 2017; Rodriguez et al. 2017).

3. Data Reduction and Analysis

3.1. HST/WFC3

We used a custom data reduction pipeline to process the HST transit observations (described in detail in Kreidberg et al. 2018b). The starting point for our reduction was the `_ima` data product provided by the Space Telescope Science Institute. These images have an intermediate level of processing, with corrections applied for dark current, linearity, and flat fielding. To extract spectra from the images, we used the optimal extraction routine of Horne (1986). This algorithm iteratively masks bad pixels in the image and provides a convenient method to reject cosmic rays from spatial scan data. To estimate the background, we identified a region of pixels that was not contaminated by flux from the target or any nearby stars (rows 10–70 and columns 400–500) and calculated the median count rate in this region. We subtracted the background and extracted the spectra from each up-the-ramp sample separately, and summed them to produce a final spectrum from the exposure. To account for spectral drift, we interpolated each spectrum to the wavelength scale of the first exposure of the first visit. The shift is applied to the final spectrum, not each up-the-ramp sample. We generated spectroscopic light curves by binning the spectra into 22 wavelength channels over the wavelength range $1.125\text{--}1.65 \mu\text{m}$. This binning corresponds to roughly five pixels in the spectral direction. The binning is about twice as coarse as the native resolution of the grism and was chosen to average over variations in sensitivity between individual pixels. Figure 1 shows the band-integrated light curve, the background counts, and the spectral shifts for each visit.

²⁷ https://irsa.ipac.caltech.edu/data/SPITZER/docs/irac/pcrs_obs.shtml

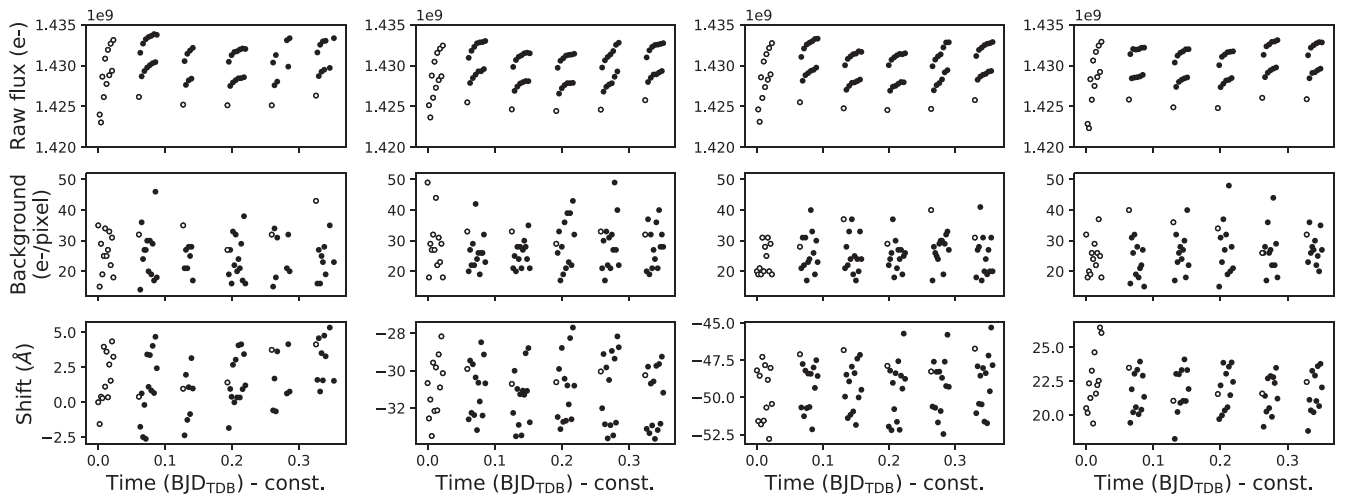


Figure 1. Diagnostic information from the HST data reduction. From top to bottom, the rows show the band-integrated raw flux, the background counts, and the wavelength shift of the spectrum relative to the first exposure of the first visit. From left to right, the columns show the four HST visits in chronological order. The open circles in the raw flux correspond to data points that we did not include in our light-curve fits due to larger amplitude instrumental ramps. The vertical offset in the top row is due to spatial scanning, which alternates between forward and reverse directions on the detector. The total counts are higher when the detector is read out in the same direction as the spatial scan.

We fit the light curves with a joint model of the transit and the instrument systematic trends. In agreement with previous work, we found that the first orbit of every visit and the first exposure in each orbit were strongly affected by a ramp-like systematic (caused by charge traps filling up in the detector; Zhou et al. 2017). This systematic is visible in the raw data, shown in Figure 1. Following past studies, we removed the first orbit of the visit and the first exposure of the remaining orbits in our analysis (e.g., Kreidberg et al. 2014). The trimmed data had three full orbits per visit of out-of-transit baseline, which is sufficient to fit for visit-long trends.

To model the transit signal, we used the `batman` package (Kreidberg 2015). For the broadband light-curve fit, the free parameters for the transit model were the ratio of planet to stellar radius R_p/R_s , the time of central transit T_c , the orbital inclination i , the ratio of semimajor axis to stellar radius a/R_s . We fixed the eccentricity to zero. We ran an initial fit with free parameters for a linear limb darkening coefficient and found excellent agreement with predictions from a Kurucz ATLAS9 stellar model with $T_{\text{eff}} = 6250$ K, $\log g = 4.5$ (cgs), and $[\text{Fe}/\text{H}] = -0.2$ (Castelli & Kurucz 2003). We therefore fixed the limb darkening on the predicted quadratic coefficients from the model for the remainder of the analysis.²⁸ For the spectroscopic channels, we fixed T_c , a/R_s , and i on the best-fit values from the broadband light curve.

To model systematic noise from the instrument, we multiplied the model transit light curve by the analytic `model-ramp` function, previously used for WFC3 data analysis (Equation (3) in Kreidberg et al. 2018b). Briefly, this function fits an exponential ramp to each orbit, a normalization constant, and a visit-long trend. For the HD 106315c data, there was no significant improvement to the light-curve fit for a quadratic term in the visit-long trend, so we used a linear term only. We also fit for a constant additive offset between scan directions. For both the broadband and spectroscopic light-curve fits, all visits were fit simultaneously. Most of the fit parameters were shared across visits, with the exception of the normalization

constant and visit-long slope, which were allowed to vary separately from visit to visit. We determined the best-fit parameters with a least-squares fitting routine and estimated parameter uncertainties with the `dynesty` package, which uses dynamic nested sampling to evaluate constant likelihood contours over the full prior volume (Speagle 2020). The light curves and best-fit models are shown in Figure 2. To ensure that we did not underestimate the uncertainties, we rescaled the per point errors from the least-squares fit such that the reduced χ^2 of the best-fit model was unity. The error bars increased by a median (mean) of 9% (12%). The `dynesty` runs were halted when the remaining contribution to the evidence was estimated to be below 0.01 of the total. The resulting median and 68% credible intervals for the transit depths are listed in Table 1. To test for correlated noise in the light curves, we binned the data in time over a range of bin sizes from 2 to 20 points and calculated the rms for each bin size (see Figure 3). The rms decreases with the square root of the number of points per bin, indicating that the noise is uncorrelated in time.

3.1.1. Independent Analysis of the WFC3 Data

We also carried out an independent data reduction and analysis. The data were reduced following the methodology previously described by Evans et al. (2016, 2017). Briefly, the spectra were extracted from each `_ima` frame by summing the difference of successive up-the-ramp samples while masking cross-dispersion regions away from the target to reject cosmic rays and nearby contaminating sources. A wavelength-independent background value was subtracted from each spectrum by taking the median pixel value in a 30×250 pixel box away from the target. Broadband light curves were produced for each visit by summing each spectrum along the full dispersion axis. The broadband light curves were fit jointly, with the systematics and transit midtimes allowed to vary separately, and R_p/R_s shared across visits. Other transit parameters such as a/R_s and i were fixed to the median values reported in Crossfield et al. (2017). For the systematics, we adopted the double-exponential ramp treatment described in de Wit et al. (2018) and also allowed the white noise to vary as a

²⁸ Calculated with the ExoCTK Limb Darkening Calculator; <https://exoctk.stsci.edu/>.

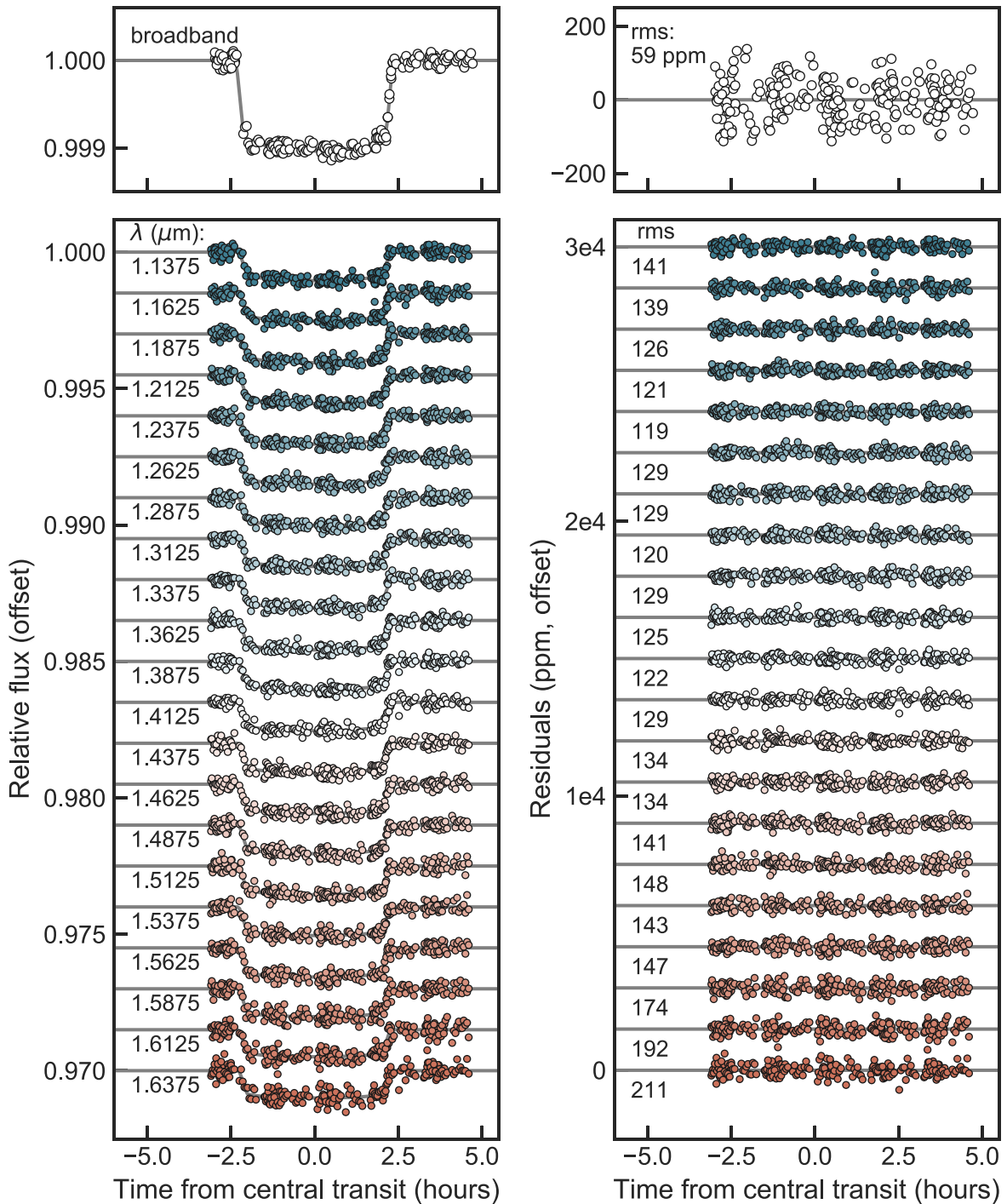


Figure 2. HST/WFC3 transit light curves. The left panel shows the phase-folded light curve from all four HST visits (points) compared to the best-fit models (lines) for the broadband light curve (top) and the spectroscopic light curve (bottom). The right panel shows the residuals from the best-fit models (right). The figure is annotated with the central wavelength for each spectroscopic light curve and the rms of the residuals (in ppm). The data are corrected for instrument systematics, normalized to an out-of-transit baseline flux of unity, and offset on the y -axis by a constant value for visual clarity.

free parameter, implemented as an increase above the formal photon noise value.

Following the broadband light-curve fit, we produced spectroscopic light curves in 14 channels spanning the 1.122–1.642 μm wavelength range following the methodology described in Evans et al. (2016), which is based on an original implementation of Deming et al. (2013). This procedure effectively removes the common-mode component of the systematics in each wavelength channel, which is dominated by

the ramp systematic. As such, for our spectroscopic light-curve fits, a simple linear time trend and variable white noise level were adequate for modeling the systematics. We also allowed R_p/R_s to vary while holding all other transit parameters fixed to the white light-curve values. In both the white light-curve and spectroscopic light-curve fits, a quadratic limb darkening law was adopted with coefficients held fixed to values determined by fitting the limb darkened profiles of an ATLAS9 stellar model with the same parameters listed in Section 3.1.

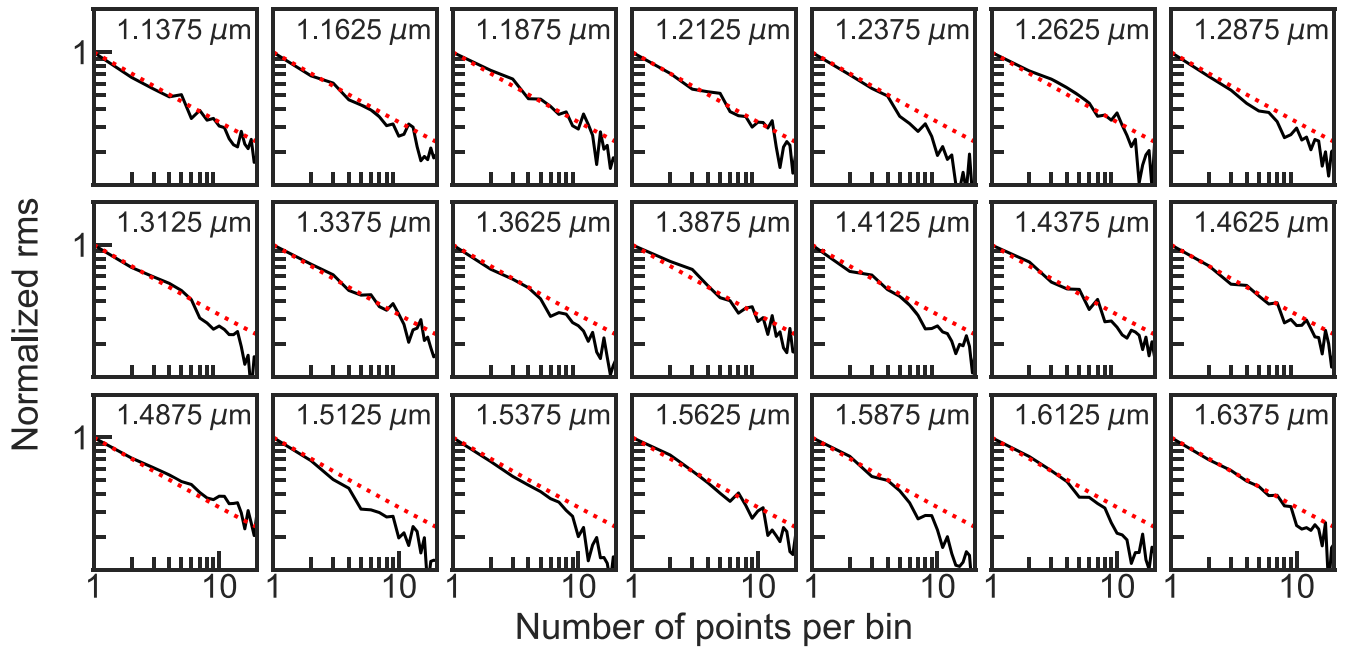


Figure 3. Allan deviation plots showing the rms variation as a function of bin size for the HST/WFC3 transit light curves. A bin size of 10 points corresponds to 30 minutes. The red dotted lines show the expected \sqrt{N} trend for photon-limited, white noise. The black lines show the measured rms for each light curve.

Table 1
Transit Depths and Limb Darkening Coefficients for the K2, HST, and Spitzer Data

| Wavelength (μm) | $(R_p/R_s)^2$ (ppm) | u_1 (fixed) | u_2 (fixed) |
|---------------------------------|------------------------|------------------|------------------|
| 0.42–0.9 | 1030 ± 26 | 0.365 | 0.244 |
| 1.125–1.150 | 1014 ± 26 | 0.180 | 0.214 |
| 1.150–1.175 | 995 ± 26 | 0.177 | 0.214 |
| 1.175–1.200 | 1022 ± 23 | 0.171 | 0.214 |
| 1.200–1.225 | 1023 ± 23 | 0.169 | 0.215 |
| 1.225–1.250 | 1006 ± 22 | 0.166 | 0.215 |
| 1.250–1.275 | 976 ± 23 | 0.162 | 0.215 |
| 1.275–1.300 | 999 ± 23 | 0.155 | 0.217 |
| 1.300–1.325 | 995 ± 21 | 0.132 | 0.230 |
| 1.325–1.350 | 1004 ± 23 | 0.148 | 0.218 |
| 1.350–1.375 | 1051 ± 23 | 0.145 | 0.216 |
| 1.375–1.400 | 1011 ± 23 | 0.140 | 0.217 |
| 1.400–1.425 | 1018 ± 24 | 0.136 | 0.216 |
| 1.425–1.450 | 1055 ± 24 | 0.132 | 0.215 |
| 1.450–1.475 | 1048 ± 23 | 0.129 | 0.213 |
| 1.475–1.500 | 1021 ± 24 | 0.123 | 0.214 |
| 1.500–1.525 | 1015 ± 25 | 0.116 | 0.214 |
| 1.525–1.550 | 1009 ± 23 | 0.112 | 0.212 |
| 1.550–1.575 | 1040 ± 27 | 0.108 | 0.208 |
| 1.575–1.600 | 997 ± 33 | 0.102 | 0.205 |
| 1.600–1.625 | 970 ± 32 | 0.096 | 0.204 |
| 1.625–1.650 | 980 ± 38 | 0.091 | 0.201 |
| 4.0–5.0 | 1070 ± 72 | 0.079 | 0.089 |

Note. The transit depth values are the median and 68% credible interval from the posterior distributions. The limb darkening parameters are precalculated from stellar models and fixed in the analysis.

The resulting transmission spectrum is compared to that of the first analysis in Figure 4. The two spectra agree to well within 1σ , and the uncertainties on the transit depths are consistent after accounting for the difference in wavelength bin size. The `model-ramp` fit has a median uncertainty on the

transit depth of 23 ppm (for $0.025 \mu\text{m}$ bins), and the common-mode fit has a median uncertainty of 17 ppm (for $0.037 \mu\text{m}$ bins). Accounting for the difference in bin size, the uncertainties agree to within 11%. Given the good agreement between the two independent analyses, we used the `model-ramp` results (listed in Table 1) for the remainder of the analysis.

3.2. Spitzer

In addition to the HST and K2 data, we also analyzed a single transit of HD 106315c observed with Spitzer in the $4.5 \mu\text{m}$ bandpass. We followed a similar approach to the one described in Berardo et al. (2019), which detrends the data using the Pixel Level Decorrelation method outlined in Deming et al. (2015). For each pixel in a frame, we first generated a time series of its flux across all frames. We then applied a median filter to each of these light curves to remove time-dependent outliers on a pixel-by-pixel basis across the entire observation. We then calculated a background level for each frame by taking the median of the flux in an annulus centered on the point-spread function. We estimated the centroid of each frame by fitting a two-dimensional Gaussian to the image, and obtained a light curve using a fixed radius aperture.

We modeled systematics in the light curve by weighting the nine brightest pixels individually as well as fitting for a quadratic time ramp. We then chose the combination of pixel coefficients, aperture size, and time-series binning that resulted in the smallest rms deviation. Time-series binning was done following the motivation and methods described in Section 3 of Deming et al. (2015). In particular, we fit to the binned data but then examined the residuals of the retrieved model when applied to the unbinned data. A minimum amount of binning is useful in removing short-term variations, which helps when fitting for long-term trends. We did not bin on timescales long enough to distort the transit signal, or where the number of data points approaches the number of free parameters. When fitting we left the photometric uncertainty as a free parameter in the

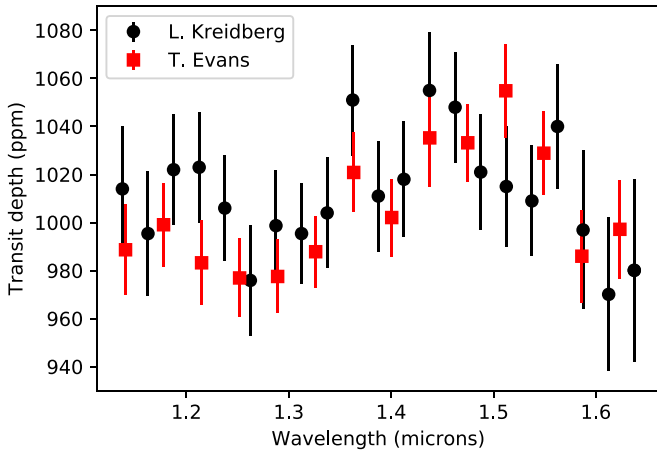


Figure 4. HST/WFC3 transmission spectra from two independent pipelines. The black circles are from the `model-ramp` analysis used by L. Kreidberg, whereas the red squares come from the common-mode error correction from T. Mikal-Evans.

Markov Chain Monte Carlo (MCMC), which accounts for the fact that the number of data points has changed. The optimal aperture radius was found to be 2.4 pixels. We used an MCMC sampler to estimate uncertainties and fit the systematic model simultaneously with a transit model from `batman` (Kreidberg 2015). We kept the period, inclination, and distance a/R_s fixed to the values 21.0564 days, $88^\circ.501$, and 26.769, respectively (based on the HST white light-curve fit), and allowed the depth and transit center to vary. We also left the uncertainty of the data points as a free parameter, which we found converged to the rms scatter of the raw light curve. We also held fixed the quadratic limb darkening parameters, which were also estimated from a Kurucz ATLAS9 stellar model. The transit light curve and best-fit model are shown in Figure 5, and the fit results are summarized in Table 2.

3.3. K2

To provide a broadband, optical-wavelength transit depth for comparison with our infrared observations, we reanalyzed the 30 minutes cadence K2 photometry of HD 106315. Although several analyses of these K2 data have already been published (Crossfield et al. 2017; Rodriguez et al. 2017), our reanalysis takes advantage of the tighter constraints on orbital parameters (a/R_s and i) provided by the high-cadence, high-precision HST observations. Our analysis used largely the same approach as described by Crossfield et al. (2017), but with a few changes. First, we used a different set of K2 photometry²⁹, which had a substantially lower rms. Second, we fixed two key orbital parameters to the following values: $a/R_s = 26.769$, and $i = 88^\circ.501$. Third, in contrast to the analysis of Crossfield et al. (2017), we allowed no dilution that would potentially decrease the observed transit depth (and so bias the analysis toward larger R_p/R_s). We neglected dilution because high-resolution imaging and spectroscopy show no nearby stars within 5 magnitudes of HD 106315 at distances of $<0''.1$ (Kosiarek et al. 2021). Finally, we held the quadratic limb darkening parameters fixed to the values predicted by an ATLAS9 stellar model ($u_1 = 0.365$ and

$u_2 = 0.244$). The transit parameters derived from this analysis are listed in Table 2.

3.4. Potential Impact of Star Spots

Unocculted star spots and plages can significantly contaminate exoplanet transmission spectra (Pont et al. 2013; Rackham et al. 2018, 2019). In general, F stars such as HD 106315 have lower spot covering fractions than stars of later spectral types (Rackham et al. 2019). The K2 light curve for HD 106315 shows variability with an amplitude of 0.1% over a timescale of 75 days, a typical value for mid-F stars (Rodriguez et al. 2017). This amplitude corresponds to a covering fraction of $0.1 \pm 0.1\%$. The expected amplitude of the stellar contamination spectrum is $0.0001\text{--}0.0002\times$ the transit depth. For the transit depth of HD 106315c (1000 ppm), the expected stellar contamination is 0.1–0.2 parts per million—a negligible contribution.

4. Atmospheric Retrieval

We carried out two independent retrieval analyses to determine the molecular abundances and cloud properties of HD 106315c’s atmosphere. We used the open-source software package `petitRADTRANS` (pRT; Mollière et al. 2019), as well as a retrieval based on the `SCARLET` framework (Benneke & Seager 2013; Benneke et al. 2019b). Both retrieval analyses used a Bayesian framework to compare the measured spectrum to one-dimensional models with variable atmospheric properties as described in this section. The analyses consistently provide tentative evidence for water vapor based on a Bayesian model comparison of retrieval models (Benneke & Seager 2013).

4.1. `petitRADTRANS` Retrieval Analysis

We used the open-source software package `petitRADTRANS` (pRT; Mollière et al. 2019), which is a fast spectral synthesis tool for exoplanet atmospheres. We connected pRT to the `PyMultiNest` tool (Buchner et al. 2014), which is a Python wrapper of the `MultiNest` (Feroz & Hobson 2008; Feroz et al. 2009, 2013) implementation of nested sampling (Skilling 2004).

The atmosphere was modeled with the vertically constant temperature and absorber mass fractions of H_2O , CH_4 , CO_2 , CO , and N_2 as free parameters. We also included the cloud-top pressure of a gray cloud deck as a free parameter. The atmospheric mean molecular weight (MMW) was calculated from the parameterized absorber abundances, assuming that the remaining mass is contributed by H_2 and He, with an H_2 :He mass ratio of 3:1. Our full model included the line opacities of H_2O , CH_4 , CO_2 , and CO , as well as the Rayleigh scattering cross sections of these species, in addition to those of H_2 , He, and N_2 . N_2 may thus be thought of as a proxy for (mostly) invisible species in the atmosphere that can increase its MMW. Instead of retrieving a reference radius at a given pressure we retrieved a reference pressure P_0 at a given radius, where we made sure that the fixed reference radius is chosen at values appropriate for placing the retrieved reference pressure values within the atmospheric pressure domain. We placed log-uniform priors on the absorber mass fractions of H_2O , CH_4 , CO_2 , CO , and N_2 between 10^{-10} and 1, requiring that the sum of all mass fractions is below unity. The temperature was allowed to vary between 400 and 1000 K. The cloud and

²⁹ <https://www.cfa.harvard.edu/~avanderb/k2.html>

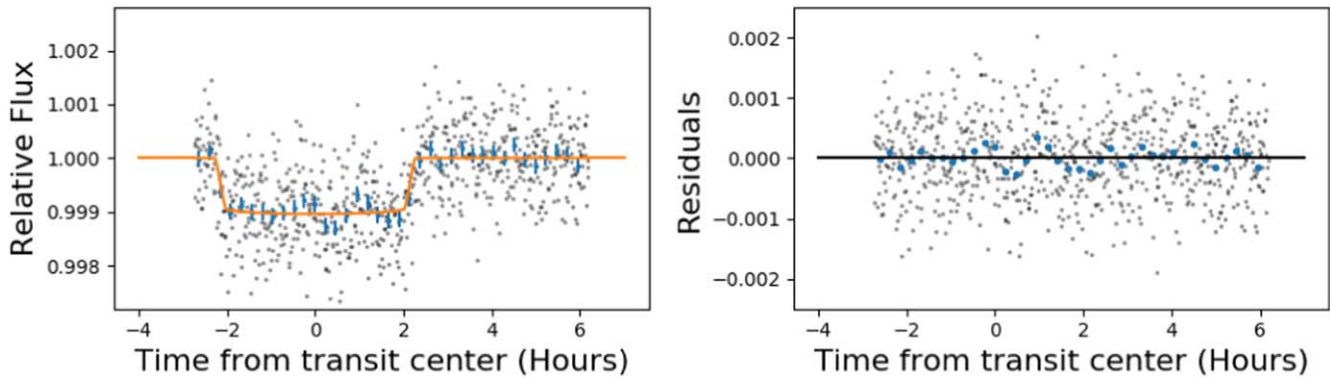


Figure 5. The light curve of HD 106315c observed with the $4.5 \mu\text{m}$ filter of Spitzer. The left panel shows the best-fit transit model to the binned light curve after removing detector systematics. The blue points with error bars are the data points binned further for visual clarity. The right-hand panel shows the residuals of the best-fit model from the data.

Table 2
K2/Spitzer Transit Parameters

| Parameter | Units | Value (K2) | Value (Spitzer) |
|-----------------|--------------------------------|---------------------------------|------------------------|
| Held fixed: | | | |
| R_s/a | ... | 0.0373566 | 0.0373566 |
| i | deg | 88.50109 | 88.50109 |
| u_1 | ... | 0.365 | 0.079 |
| u_2 | ... | 0.244 | 0.089 |
| Derived values: | | | |
| T_0 | BJD _{TDB} - 2,454,833 | $2778.1320^{+0.0016}_{-0.0017}$ | 3030.8079 ± 0.0012 |
| P | d | 21.0564 ± 0.0024 | 21.0564 (fixed) |
| R_p/R_s | % | 3.208 ± 0.041 | 3.271 ± 0.11 |
| $(R_p/R_s)^2$ | ppm | 1030 ± 26 | 1070 ± 75 |

reference pressure could be placed at any location within the atmospheric pressure domain, imposing a log-uniform prior. However, we note that the posterior distribution for the water abundance (which is the only species we detect tentatively) is sensitive to the choice of prior bounds, particularly if regions are explored that do not produce any difference in the model spectrum (for example, very deep clouds). We additionally tested retrieving a scattering haze ($\kappa_{\text{haze}} = \kappa_0[\lambda/\lambda_0]^\gamma$), a cloud patchiness parameter (mixing clear and cloudy terminators), and the planet’s gravity within measurement uncertainties, but none of these tests significantly changed our results.

In order to test how reliably water can be detected in our spectrum we followed the approach introduced in Benneke & Seager (2013). Our full model retrieved the abundance of all absorbers listed above. Then, we iteratively removed one absorber at a time and reran the retrieval. Comparing the evidences between the full model and the model lacking a given species allows us to assess whether the observation is in favor of that species being included in the model. The retrieved atmospheric properties for the full model are shown in Figure 6.

The resulting evidences Z are listed in Table 3. The Bayes factor is the ratio of evidences. Bayes factors greater than 100 are considered decisive, 10–100 are strong, 3.2–10 are substantial, and below 3.2 are insignificant (Kass & Raftery 1995). None of the tested species is substantially favored to be included in our model. However, the full model is slightly favored when compared to a model that removed H_2O , with a Bayes factor of 1.7. The fact that water is the only molecule that can lead to noticeable differences in the fit is not

surprising, since WFC3 spectra are predominantly sensitive to absorption from H_2O . Higher precision measurements of the transmission spectrum are needed to uniquely identify absorbing species in the atmosphere of HD 106315c.

The retrieved spectrum is shown in Figure 7. The amplitude of spectral features in the best-fit model is about 30 ppm ($7\times$ smaller than that expected for a solar composition, cloud-free atmosphere). This observed peak-to-trough amplitude corresponds to 0.8 ± 0.04 H_2/He scale heights (assuming $\mu = 2.3$ atomic mass units, $T = 800$ K, and $g = 6.0 \text{ m s}^{-2}$). In general, to produce features of this amplitude, models have (1) an enhanced MMW (which decreases the atmospheric scale height and shrinks the spectral features), (2) high-altitude clouds, which truncate the spectral feature at the cloud deck altitude, or (3) both of the above (Benneke & Seager 2013). In the case of HD 106315c, the retrieval prefers scenarios (2) and (3), with the highest posterior probability for moderate cloud coverage. A broad range of H_2O abundances is consistent with the data (3×10^{-4} – $290\times$ solar at 1σ). The “solar” water abundance corresponds to the chemical equilibrium water volume mixing ratio for a solar composition gas at 1 mbar pressure and 800 K (2.2×10^{-4}). The cloud-top pressure is in the range $P_{\text{cloud}} = 0.04$ – 130 mbar (at 1σ). There is some degeneracy between $n_{\text{H}_2\text{O}}$ and P_{cloud} , because a higher water abundance pushes the photosphere to lower pressures. There is also a tail of probability toward water-rich solutions with deep clouds (below the observable photosphere). Very high water abundances cannot be ruled out ($n_{\text{H}_2\text{O}} < 2100\times$ solar at 2σ confidence, $n_{\text{H}_2\text{O}} < 4200\times$ solar at 3σ). At these high

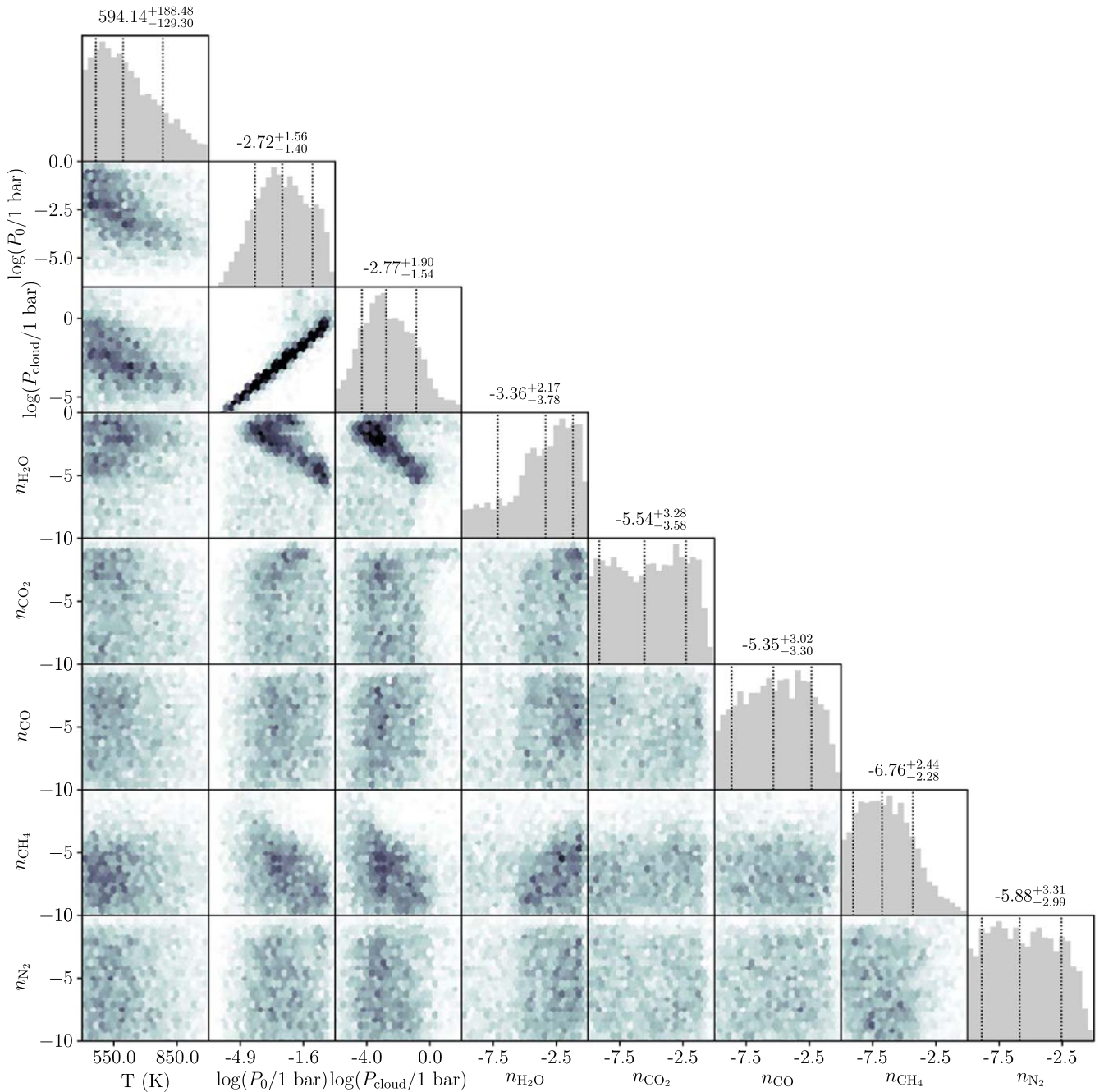


Figure 6. The retrieved atmospheric properties for the full retrieval with petitRADTRANS. The panels show the posterior distribution of parameters from the nested sampling run. Darker shading corresponds to higher posterior probability. The diagonal shows a one-dimensional histogram for each parameter, with dotted lines denoting the median and 1σ credible interval. The molecular abundances are the logarithm (base 10) of their volume mixing ratio. For reference, a solar composition gas at 1 mbar pressure and 800 K has $n_{\text{H}_2\text{O}} = -3.65$, $n_{\text{CO}_2} = -6.32$, $n_{\text{CO}} = -3.37$, $n_{\text{CH}_4} = -4.43$, and $n_{\text{N}_2} = -4.23$.

Table 3
Bayesian Evidence for Atmospheric Retrievals with PetitRADTRANS

| Retrieval model | $\Delta \ln(Z)$ | Bayes factor for molecule present |
|---------------------|--------------------|-----------------------------------|
| no H ₂ O | $+0.517 \pm 0.078$ | 1.68 |
| no CO ₂ | -0.347 ± 0.085 | 0.71 |
| no CO | -0.490 ± 0.122 | 0.61 |
| no CH ₄ | -0.482 ± 0.040 | 0.62 |
| no N ₂ | -0.766 ± 0.237 | 0.46 |
| no cloud | $+0.022 \pm 0.067$ | 1.02 |

metallicities, the atmosphere is no longer dominated by H₂, but rather by H₂O or CO₂ (Moses et al. 2013).

4.2. SCARLET Retrieval Analysis

As an independent check of the results from petitRADTRANS, we also interpreted the transmission spectrum with the SCARLET atmospheric retrieval framework (e.g., Benneke & Seager 2012, 2013; Knutson et al. 2014; Kreidberg et al. 2014; Benneke 2015; Benneke et al. 2019a, 2019b; Wong et al. 2020). Employing SCARLET’s free molecular composition

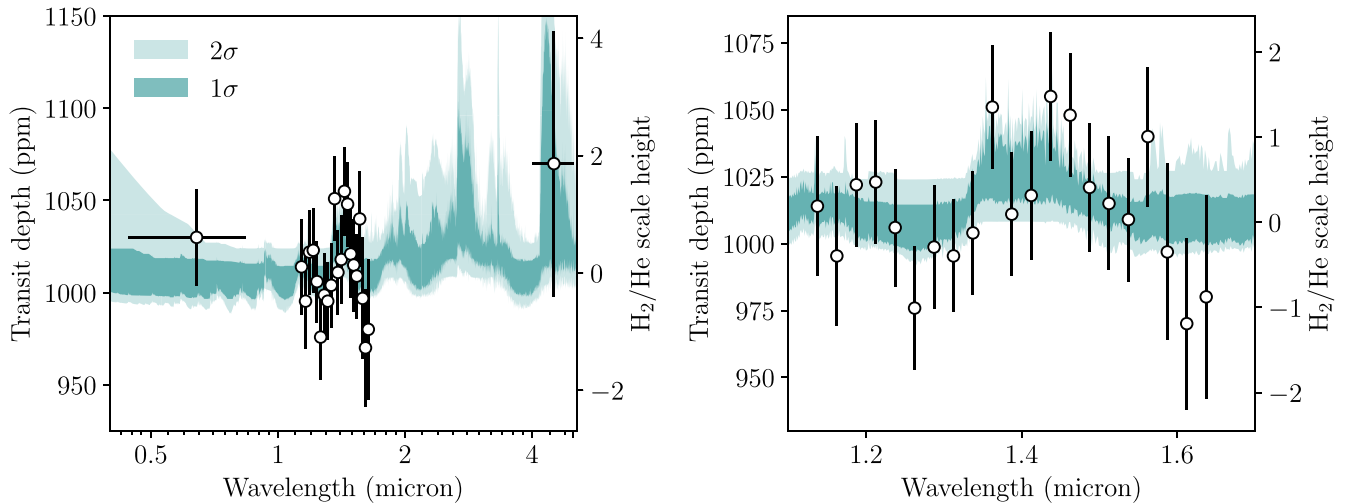


Figure 7. The transmission spectrum of HD 106315c (points with 1σ uncertainties) compared to retrieved spectra from the FULL model (teal shading) with petitRADTRANS. The H_2/He atmospheric scale height is indicated on the right y-axis, assuming a solar composition atmosphere at the planet’s equilibrium temperature (the true scale height is likely smaller, due to enhanced metallicity and/or lower temperature). The tentative detection of water absorption is driven by the small increase in transit depth near $1.4\ \mu\text{m}$.

mode we defined the mole fractions of H_2O , CH_4 , CO_2 , CO , and N_2 as free parameters and assumed a well-mixed atmosphere. The remainder of the atmosphere gas was assumed to be composed of H_2 and He in the solar abundance ratio. We included a gray cloud deck using a free parameter describing the cloud-top pressure, and an additional free parameter to capture our prior ignorance of the temperature in the photosphere of HD 106315c near the terminator.

To evaluate the likelihood for a particular set of atmospheric parameters, the SCARLET forward model in free molecular composition mode computes the hydrostatic equilibrium and line-by-line radiative transfer. We considered the latest line opacities of H_2O , CO , and CO_2 from HiTemp (Rothman et al. 1998) and CH_4 from ExoMol (Tennyson et al. 2016), as well as the collision-induced absorption of H_2 and He. We employed log-uniform priors between 10^{-10} and $10^{-0.5} = 31\%$, but required that the sum of all mass fractions is below unity. We employed log-uniform priors for the cloud-top pressures 10^{-3} and 10^7 Pa. We used a uniform prior on the photospheric temperature between 620 and 1150 K (70%–130% of the equilibrium temperature).

SCARLET then determined the posterior constraints by combining the SCARLET atmospheric forward model with nested sampling (Skilling 2004). We ran the analyses well beyond formal convergence to obtain a smooth posterior distribution and capture the contours of the wide parameter space in agreement with the transmission spectrum of HD 106315c. As in Section 4.1, we evaluated the presence of individual molecular species in the atmosphere of HD 106315c following the strategy outlined in Benneke & Seager (2013).

The retrieval results are shown in Figure 8. Our analysis reveals a Bayes factor of 2.6 in favor of the presence of water vapor in the atmosphere of HD 106315c, which can be regarded as tentative evidence. No other molecular species is favored by the data. We also tested for the presence of clouds by comparing the full retrieval model to a model that lacks clouds in the hypothesis space, but find no evidence in the observational data. The small variation in evidence computed with SCARLET versus petitRADTRANS is most likely due to the slight differences in prior volume for the two analyses. We

performed the final parameter estimation using the full retrieval model including the five molecules (H_2O , CH_4 , CO_2 , CO , and N_2) and gray clouds. The best-fitting model matches all data points within their 1σ uncertainties. A wide range of models is consistent with the data, in agreement with the results from petitRADTRANS.

5. Cloud and Haze Models

The retrieval analysis from the previous section showed that the muted water feature in the transmission spectrum is consistent with a low-metallicity composition with high-altitude condensates. To explore what condensate properties are plausible for HD 106315c, we ran forward models with physically motivated cloud and haze opacity values.

5.1. Cloud Models

Transmission spectra including the effect of clouds were calculated following the methodology of Morley et al. (2015, 2017). First, 1D cloud-free model temperature profiles were calculated, assuming both radiative–convective and chemical equilibrium, using the approach described in detail in McKay et al. (1989), Marley & McKay (1999), Saumon & Marley (2008), and Fortney et al. (2008). We calculated profiles for metallicities of $[\text{M}/\text{H}] = 0.0, 0.5, 1.0, 1.5, 2.0,$ and 2.5 (1, 3, 10, 30, 100, and $300\times$ solar). The opacity database is described in detail in Freedman et al. (2008, 2014), with updated chemical equilibrium calculations and opacities as described in Marley et al. (2021).

We included the condensation of Na_2S , KCl , and ZnS , which are expected to condense at the temperature of HD 106315c ($T_{\text{eq}} = 800$ K). We calculated cloud altitude and height along the cloud-free pressure–temperature profile; the cloud properties were calculated using the methods described in Ackerman & Marley (2001) and Morley et al. (2012) for each metallicity, assuming a range of sedimentation efficiencies ($f_{\text{sed}} = 2, 1, 0.5,$ and 0.1), a parameter which controls the cloud particle size and cloud height. This model calculates the cloud optical depth, single-scattering albedo, and asymmetric parameter for each

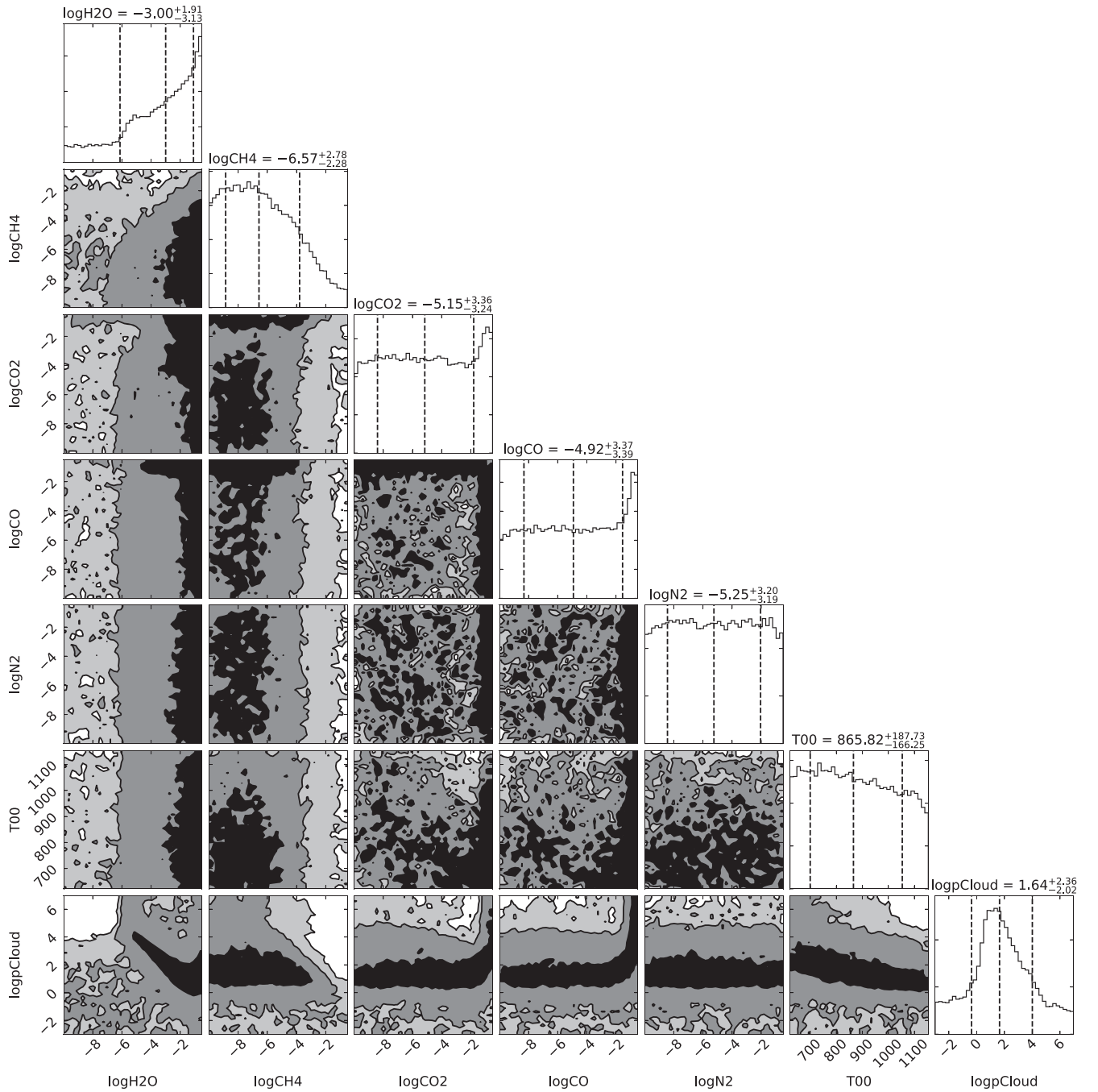


Figure 8. Molecular abundance and cloud property constraints from the SCARLET free retrieval analysis. The top panels in each column show the 1D marginalized posterior distributions of the molecular abundances and cloud properties, with dashed vertical lines in the histograms indicating the marginalized 16th, 50th, and 84th credible intervals. The subjacent 2D panels show the correlations among the gases and cloud properties, with the black, dark gray, and light gray regions corresponding to the 1σ (39.3%), 2σ (86.5%), and 3σ (98.9%) credible intervals. The cloud pressure is given in logarithm (base 10) Pascals, and the abundances are given as the logarithm (base 10) of their volume mixing ratio.

layer of the atmosphere. Example pressure–temperature profiles with cloud condensation curves are shown in Figure 9.

To calculate transmission spectra, we used the transmission spectrum model described in the Appendix of Morley et al. (2017). Gas opacity from H_2 collisionally induced absorption, CO_2 , H_2O , CH_4 , CO , NH_3 , PH_3 , H_2S , Na , K , TiO , VO , and HCN were included. We calculated models for each metallicity and f_{sed} combination considered.

Figure 10 shows the goodness of fit for the cloudy model grid compared to the WFC3 transmission spectrum. The K2 and Spitzer data are not precise enough to significantly affect the goodness of fit. The best fits have small water absorption features with an amplitude of around 30 ppm. The amplitude of features in the models is a trade-off between metallicity and cloud altitude: higher metallicity models tend to have a smaller scale height and thus smaller features. A lower sedimentation efficiency also decreases the feature amplitude. Small f_{sed}

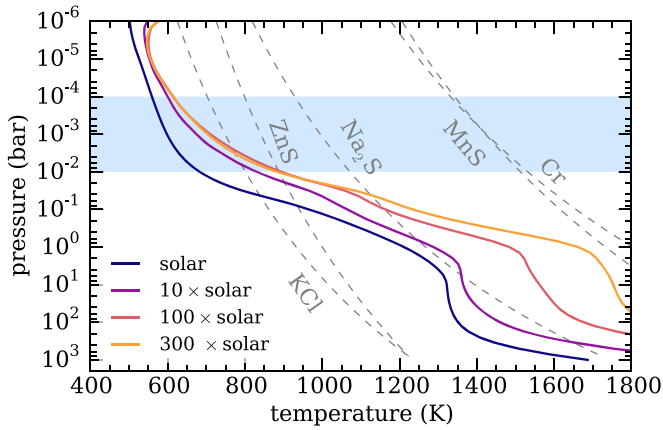


Figure 9. Pressure–temperature profiles (solid lines) for HD 106315c compared to condensation curves for expected cloud species (dashed lines). The models are assumed to be in radiative–convective and chemical equilibrium. The condensation curves are calculated for a 100× solar metallicity composition; for lower metallicities, the condensation curves shift left (by approximately 100 K per 1 dex metallicity). The shaded region marks the range of pressures that transmission spectroscopy is sensitive to, assuming 100× solar metallicity.

values loft cloud particles higher in the atmosphere, obscuring spectral features. As shown in Figure 9, the cloud base is typically below the pressure level sensed by the observations, so f_{sed} values of $\lesssim 0.5$ are required to loft the cloud into the observable atmosphere. For the HD 106315c spectrum, the best-fit models are high-metallicity atmospheres (100–300× solar), or lower metallicity with high-altitude clouds ($f_{\text{sed}} < 0.5$).

5.2. Haze Models

We also calculated transmission spectra for hazy atmospheres using the photochemistry, microphysics, and transmission spectrum models of Kawashima & Ikoma (2018) in the same way as in Kawashima et al. (2019) and Kawashima & Ikoma (2019). We first performed photochemical simulations to derive the steady-state distribution of gaseous species. Then, since the haze monomer production rate is uncertain for exoplanets, we assumed a certain fraction of the sum of the photodissociation rates of the major hydrocarbons in our photochemical model, CH_4 , HCN , and C_2H_2 , would result in haze monomer production. We call this fraction the haze formation efficiency f_{haze} following Morley et al. (2013). With this assumption, we derived the steady-state distribution of haze particles by microphysical simulations. Finally, we modeled transmission spectra of the atmospheres with the obtained profiles of haze particles and gaseous species.

For the temperature–pressure profile, we used the online available³⁰ analytical model of Parmentier & Guillot (2014) assuming an internal temperature of 100 K and their correction factor of 0.25, which corresponds to the case where the irradiation is efficiently redistributed over the entire planetary surface. For the other input parameters, we used the default opacities (Valencia et al. 2013; Parmentier et al. 2015) and Bond albedo. We included convection. Solar elemental abundance ratios were taken from Lodders (2003). For the UV spectrum of HD 106315, we used that of the Sun from Segura et al. (2003) because of its similar stellar type (F5;

Houk & Swift 1999). We assumed a constant eddy diffusion coefficient of $10^7 \text{ cm}^2 \text{ s}^{-1}$ throughout the atmosphere for both photochemistry and microphysics calculations. We assumed a monomer radius of 1 nm and an internal density of haze particles of 1 g cm^{-3} . The refractive index of haze is uncertain for exoplanets, so we considered two representative cases, tholin (Khare et al. 1984) and soot (Hess et al. 1998).

We calculated spectra for 1, 10, and 100× solar metallicity atmospheres with a range of f_{haze} from 10^{-7} to 1 in 1 dex increments. The integrated monomer production rate for $f_{\text{haze}} = 1$ (the sum of the photodissociation rates of CH_4 , HCN , and C_2H_2) becomes smaller with increasing metallicity: 1.71×10^{-10} , 1.20×10^{-10} , and $5.51 \times 10^{-11} \text{ g cm}^2 \text{ s}^{-1}$ for 1, 10, and 100× the solar metallicity atmospheres, respectively.

For the calculation of transmission spectra, we treated the reference radius at 10 bar pressure level as a parameter. We found the appropriate value with a grid of 0.1% of the observed transit radius, which yields the minimum reduced χ^2 with 18 degrees of freedom (21 data points minus 3 free parameters of metallicity, f_{haze} , and reference radius), for each case. We accounted for the transmission curve of the WFC3 G141 grism from the SVO Filter Profile Service³¹ (Rodrigo et al. 2012; Rodrigo & Solano 2013).

The left panel of Figure 11 shows several representative models compared to the measured WFC3 spectrum: models for clear atmospheres of three different metallicities, as well as hazy (tholin) atmospheres with haze formation efficiency tuned to fit the WFC3 data well. The error bars for the K2 and Spitzer points are large and therefore have a negligible effect on the goodness of fit. The right panel of Figure 11 shows the goodness of fit for the model grids. We find that modest haze formation efficiencies of 10^{-3} – 10^{-4} generally match the observed spectra for all the three different metallicities, for both tholins and soots. This is because a smaller scale height due to increasing metallicity can be compensated for by a smaller fiducial monomer production rate. Overall, these haze production efficiencies are orders of magnitude lower than the extreme values required to reproduce the featureless spectrum of GJ 1214b (Morley et al. 2015; Kawashima et al. 2019). As noted above, the near-UV irradiation of HD 106315c is likely higher than that of GJ 1214b, so more haze precursors are present and a lower haze production efficiency is needed. Broadly speaking, the cloud and haze models are qualitatively similar over the wavelength range of our data, and either model can explain the spectrum. However, previous work has shown that clouds and hazes affect the spectrum differently at different wavelengths (Morley et al. 2015). In particular, small haze particles may lead to strong slopes in the optical and larger differences between optical and infrared wavelengths than cloud models. Future observations over a wider wavelength range would help distinguish between the two possibilities for HD 106315c.

6. Interior Structure Models

Comparison between interior structure and envelope metallicity can provide additional constraints on the bulk composition of the planet (Kreidberg et al. 2018b; Thorngren & Fortney 2019). For example, given knowledge of the envelope metallicity, it is possible to put limits on the core mass, which otherwise suffers from a large degeneracy for planets in the

³⁰ <http://cdsarc.u-strasbg.fr/viz-bin/qcat?J/A+A/562/A133>

³¹ <http://svo2.cab.inta-csic.es/theory/fps/>

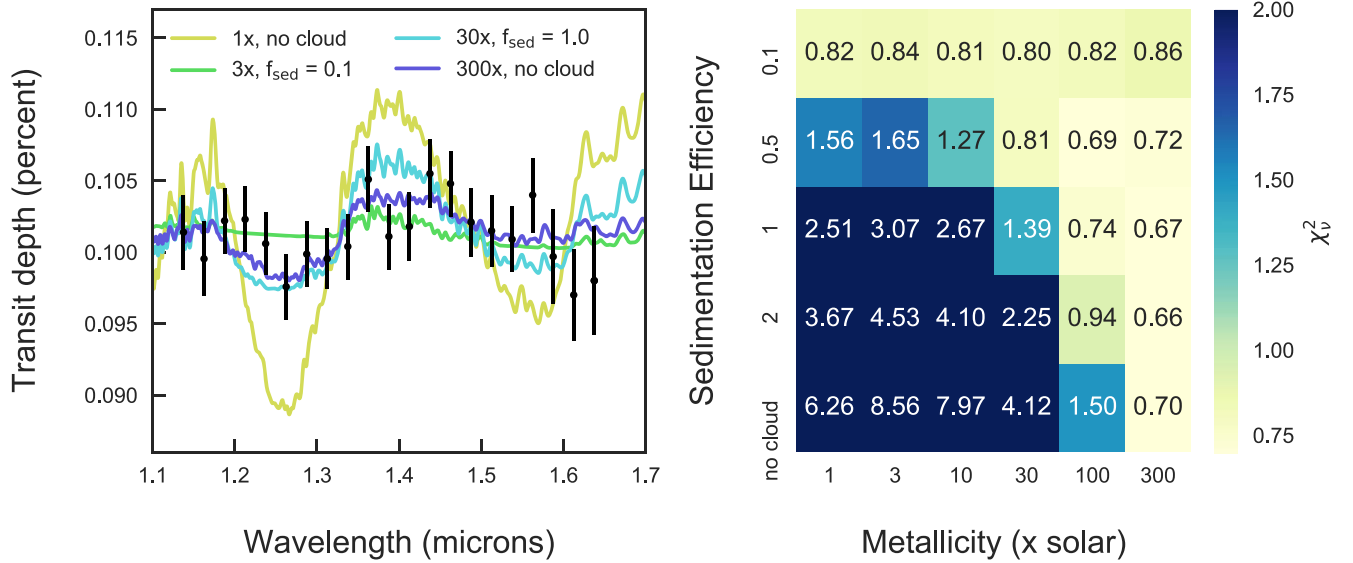


Figure 10. A sample of cloud forward models compared to the observed WFC3 spectrum (left) and a goodness of fit for the full grid of cloudy models (right). The grid cell shading indicates the reduced χ^2 of the fit to the WFC3 data. The fit has 18 degrees of freedom (21 data points, free parameters for metallicity, f_{sed} , and reference radius).

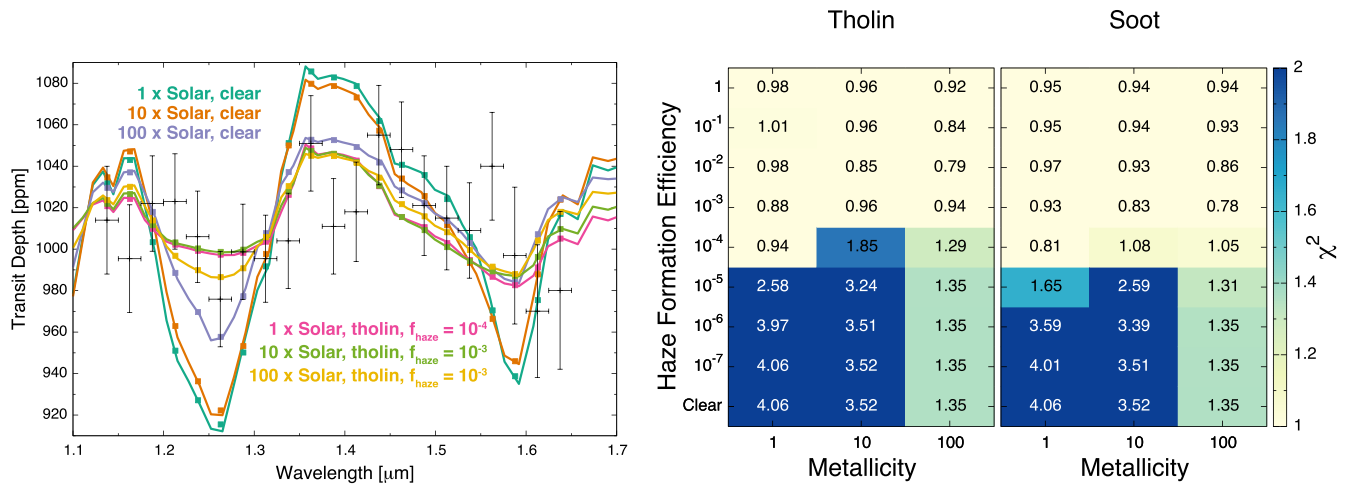


Figure 11. Left: representative haze forward models compared to the measured WFC3 spectrum; models for the clear atmospheres of 1 (dark green line), 10 (orange line), and 100 (purple line) \times solar metallicity, and those for the hazy (tholin) atmospheres of 1 (pink line), 10 (light green line), and 100 (yellow line) \times solar metallicity. The haze formation efficiency that fits the observed data well is chosen. Right: goodness of fit for the full grid of tholin and soot models. The grid cell shading indicates the reduced χ^2 of the fit to the WFC3 data. The fit has 18 degrees of freedom (21 data points, free parameters for metallicity, f_{haze} , and reference radius).

2–5 R_{\oplus} radius range (Rogers & Seager 2010). We evaluated the internal structure of HD 106315c with a model consisting of an inner core and an H/He outer envelope enriched with various amounts of water and rock (in a 50:50 ratio), using the methods described by Thorngren et al. (2016). We explored two limiting cases for the core composition: one is composed entirely of isothermal rock with radioactive heating, and the other is composed of convective water. Using the observed mass (with error), radius (with error), age (with error), and flux (ignoring error), we retrieved the core mass over a range of envelope metallicities. Our results are shown in Figure 12.

In the absence of any information about the envelope composition, the core mass fraction for HD 106315c could range anywhere from 0 to 1. The higher the envelope metallicity, the lower the core mass fraction required to explain the observed mass, radius, and age of the planet. To help break

this degeneracy, we compared the results from the atmospheric retrieval with the interior structure model (using water abundance as a proxy for envelope metallicity). The retrieval results are shown alongside the interior structure model in Figure 12. Using the retrieved abundance of H_2O from petitRADTRANS as a proxy for the envelope metallicity (5×10^{-4} – $290 \times$ solar at 1σ confidence), we estimate that the core mass fraction is greater than 30% regardless of the core composition (rock or ice). These conclusions generally resemble our understanding of the bulk composition of Uranus and Neptune, which are expected to have a core mass of 80%–90% (Hubbard et al. 1991; Fortney & Nettelmann 2010; Nettelmann et al. 2013). Follow-up atmosphere characterization with a higher precision and broader wavelength coverage can further constrain the envelope metallicity and core mass of HD 106315c.

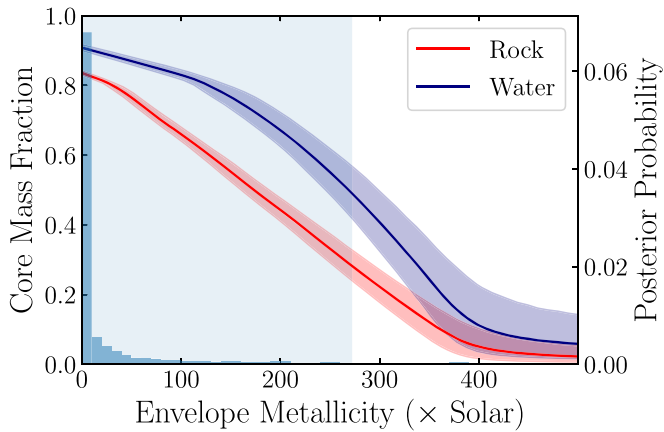


Figure 12. Core fraction vs. envelope metallicity from interior structure modeling for a rocky core (red line with 1σ uncertainty shaded) and a water core (blue line with 1σ uncertainty). The retrieval results for the envelope metallicity are overplotted as a histogram, with the 1σ credible interval indicated by the blue shaded region.

7. Discussion and Conclusions

The number of small exoplanets with precise transmission spectra is growing, and already the population shows diversity in atmospheric properties. Some appear to have envelope metallicities below that of Neptune (e.g., HAT-P-26b; Wakeford et al. 2017), whereas others require a higher metallicity (GJ 436b; Morley et al. 2017). Some planets are blanketed with thick high-altitude clouds or haze (particularly GJ 1214b; Kreidberg et al. 2014), while others have deeper condensates or even cloud-free atmospheres (Benneke et al. 2019b; Madhusudhan et al. 2020). This diversity is expected from theoretical models. For example, planet population synthesis predicts a wide range of envelope enrichment for sub-Neptunes (e.g., Fortney et al. 2013). Similarly, cloud and haze models indicate that condensate properties may vary widely across different planets. Condensate formation depends on many different atmospheric properties (e.g., temperature, metallicity, UV irradiation, and vertical mixing) so there is no one-size-fits-all model to predict whether an atmosphere is cloudy or clear at the pressure levels sensed by transmission spectroscopy (Morley et al. 2015; Gao & Benneke 2018; He et al. 2018; Hörst et al. 2018; Kawashima et al. 2019; Ohno et al. 2020).

Where does HD 106315c fit into this diverse picture? The small amplitude of spectral features is consistent with that of other sub-Neptunes, which all have feature amplitudes attenuated relative to expectations for solar composition, cloud-free atmospheres (Crossfield & Kreidberg 2017). Intriguingly, the amplitude of spectral features (0.8 ± 0.04 H₂/He scale heights) agrees well with the demographic trend noted in Crossfield & Kreidberg (2017) and Libby-Roberts et al. (2020), which shows an increase in the amplitude of the WFC3 water feature with planet equilibrium temperature. This is a somewhat surprising finding, because there are many factors (noted above) that affect the observed spectral feature amplitude for planets in this population. A further demographic study of water absorption in sub-Neptunes will be explored in a follow-up paper.

The tentative water detection for HD 106315c is consistent with a wide range of abundances (3×10^{-4} – $290\times$ solar at 1σ confidence), and is most comparable to that estimated for

HAT-P-11b and K2-18b (Fraine et al. 2014; Benneke et al. 2019b; Chachan et al. 2019). Low metallicities ($<50\times$ solar), akin to those GJ 3470b, HAT-P-26b, and WASP-107b (Wakeford et al. 2017; Kreidberg et al. 2018a; Benneke et al. 2019a) are possible for HD 106315c, provided it has some condensates in its atmosphere that truncate the amplitude of the water feature. The condensate properties are modest relative to extremes such as GJ 1214b, which has a featureless spectrum requiring either very low sedimentation efficiency clouds and high atmospheric metallicity ($f_{\text{sed}} \leq 0.1$ and $1000\times$ solar composition), or very efficient photochemical haze production ($\gtrsim 10\%$ efficiency) for a $50\times$ solar metallicity composition (Kreidberg et al. 2014; Morley et al. 2015). For comparison, the transmission spectrum of HD 106315c is fit well with $f_{\text{sed}} \leq 0.5$ or haze production efficiencies of 10^{-3} – 10^{-4} .

The tentative detection of a small water feature in HD 106315c makes it an intriguing candidate for follow-up observations. While the amplitude of spectral features may be small, it would be valuable to pursue additional measurements because of the unique properties of the HD 106315 system relative to other observationally accessible exo-Neptunes. HD 106315 has two planets with low obliquities, suggestive of a gentle disk migration or even in situ formation (Zhou et al. 2018). By contrast, most of the best-studied planets in this size range have highly misaligned orbits more suggestive of inward scattering (e.g., HAT-P-11b, WASP-107b, and GJ 436b). By studying the atmospheres of the planets, it may be possible to distinguish between these migration pathways (Madhusudhan et al. 2014). In addition to the planetary architecture, HD 106315 is also an unusual host star: it is more massive than the typical M-dwarf hosts, enabling more precise age and radius determinations that are key inputs for interior structure models. Continued observations of HD 106315c will therefore be complementary to those of other benchmark exo-Neptunes.

Infrared observations are a particularly promising avenue—spectroscopy in the 4–5 μm range is sensitive to absorption from CO₂, a prominent feature expected in high-metallicity atmospheres (Moses et al. 2013). If the atmosphere has a lower metallicity but is cloudy/hazy, infrared observations are also promising because the condensates may have a lower opacity at longer wavelengths (e.g., GJ 3470b; Benneke et al. 2019b). Clouds and haze are also expected to have distinct optical properties in the infrared (Morley et al. 2015). Future transmission spectroscopy observations with JWST could potentially distinguish between these possibilities (Greene et al. 2016) and confirm whether HD 106315c does indeed have a Neptune-like core mass and envelope composition. If it does, that will provide new incentive for formation models to produce ice giants on a wide range of orbits from 0.15 au (that of HD 106315c) to 30 au (that of Neptune). As a final note, while HD 106315c provides an interesting point of comparison with Neptune in our own solar system, it does have some notable differences, particularly its short-period orbit. Sub-Jovian exoplanets that are close to their host stars are susceptible to photoevaporative mass loss due to incident high-energy stellar irradiation (e.g., Lopez & Fortney 2013; Owen & Wu 2013). This mass loss may be substantial (10%) for planets with a comparable surface gravity and irradiation to HD 106315c; however, there are large uncertainties in the mass loss due to the unknown early X-ray and ultraviolet flux of the star, the planets’ migration history, the mass-loss efficiency, and other factors. The mass loss may affect the atmospheric

composition: while heavier elements are expected to be dragged away along with escaping H_2 , if enough of the envelope is lost, it would expose deeper layers that could have a higher metallicity (Fortney et al. 2013). While the current transmission spectrum presented here does not constrain the atmospheric composition well enough to make possible a meaningful comparison with Neptune, these caveats are important to bear in mind for future observations for HD 106315c and other small planets.

Support for HST program GO-15333 was provided by NASA through a grant from the Space Telescope Science Institute, which is operated by the Association of Universities for Research in Astronomy, Inc., under NASA contract NAS 5-26555. This work is based (in part) on observations made with the Spitzer Space Telescope, which was operated by the Jet Propulsion Laboratory, California Institute of Technology under a contract with NASA. This research has made use of the SIMBAD database, operated at CDS, Strasbourg, France. Some of the data presented in this paper were obtained from the Mikulski Archive for Space Telescopes (MAST). Support for MAST for non-HST data is provided by the NASA Office of Space Science via grant NNX13AC07G and by other grants and contracts. This research made use of matplotlib, a Python library for the publication of quality graphics (Hunter 2007). This research made use of SciPy (Virtanen et al. 2020). This research made use of NumPy (van der Walt et al. 2011). P.M. acknowledges support from the European Research Council under the European Union's Horizon 2020 research and innovation program under grant agreement No. 832428. Y.K. acknowledges support from the European Union's Horizon 2020 Research and Innovation Programme under Grant Agreement 776403. M.R.K. is supported by the NSF Graduate Research Fellowship, grant No. DGE 1339067. L.K. acknowledges M.R. Line for illuminating discussions.

Software: petitRADTRANS (Mollière et al. 2019), PyMultiNest (Buchner et al. 2014), batman (Kreidberg 2015), dynesty (Speagle 2020).

ORCID iDs

Laura Kreidberg  <https://orcid.org/0000-0003-0514-1147>
 Paul Mollière  <https://orcid.org/0000-0003-4096-7067>
 Daniel P. Thorngren  <https://orcid.org/0000-0002-5113-8558>
 Yui Kawashima  <https://orcid.org/0000-0003-3800-7518>
 Caroline V. Morley  <https://orcid.org/0000-0002-4404-0456>
 Björn Benneke  <https://orcid.org/0000-0001-5578-1498>
 Thomas Mikal-Evans  <https://orcid.org/0000-0001-5442-1300>
 David Berardo  <https://orcid.org/0000-0001-6298-412X>
 Molly R. Kosiarek  <https://orcid.org/0000-0002-6115-4359>
 Varoujan Gorjian  <https://orcid.org/0000-0002-8990-2101>
 David R. Ciardi  <https://orcid.org/0000-0002-5741-3047>
 Jessie L. Christiansen  <https://orcid.org/0000-0002-8035-4778>
 Diana Dragomir  <https://orcid.org/0000-0003-2313-467X>
 Courtney D. Dressing  <https://orcid.org/0000-0001-8189-0233>
 Jonathan J. Fortney  <https://orcid.org/0000-0002-9843-4354>
 Benjamin J. Fulton  <https://orcid.org/0000-0003-3504-5316>
 Thomas P. Greene  <https://orcid.org/0000-0002-8963-8056>

Kevin K. Hardegree-Ullman  <https://orcid.org/0000-0003-3702-0382>
 Andrew W. Howard  <https://orcid.org/0000-0001-8638-0320>
 Steve B. Howell  <https://orcid.org/0000-0002-2532-2853>
 Howard Isaacson  <https://orcid.org/0000-0002-0531-1073>
 Jessica E. Krick  <https://orcid.org/0000-0002-2413-5976>
 John H. Livingston  <https://orcid.org/0000-0002-4881-3620>
 Joshua D. Lothringer  <https://orcid.org/0000-0003-3667-8633>
 Farisa Y. Morales  <https://orcid.org/0000-0001-9414-3851>
 Erik A. Petigura  <https://orcid.org/0000-0003-0967-2893>
 Joseph E. Rodriguez  <https://orcid.org/0000-0001-8812-0565>
 Joshua E. Schlieder  <https://orcid.org/0000-0001-5347-7062>
 Lauren M. Weiss  <https://orcid.org/0000-0002-3725-3058>

References

- Ackerman, A. S., & Marley, M. S. 2001, *ApJ*, 556, 872
 Atreya, S. K., Hofstadter, M. H., In, J. H., et al. 2020, *SSRv*, 216, 18
 Benneke, B. 2015, arXiv:1504.07655
 Benneke, B., Knutson, H. A., Lothringer, J., et al. 2019a, *NatAs*, 3, 813
 Benneke, B., & Seager, S. 2012, *ApJ*, 753, 100
 Benneke, B., & Seager, S. 2013, *ApJ*, 778, 153
 Benneke, B., Wong, I., Piaulet, C., et al. 2019b, *ApJL*, 887, L14
 Berardo, D., Crossfield, I. J. M., Werner, M., et al. 2019, *AJ*, 157, 185
 Buchner, J., Georgakakis, A., Nandra, K., et al. 2014, *A&A*, 564, A125
 Castelli, F., & Kurucz, R. L. 2003, in IAU Symp. 210, Modelling of Stellar Atmospheres, ed. N. Piskunov, W. W. Weiss, & D. F. Gray (San Francisco, CA: ASP), A20
 Chachan, Y., Knutson, H. A., Gao, P., et al. 2019, *AJ*, 158, 244
 Coughlin, J. L., Mullally, F., Thompson, S. E., et al. 2016, *ApJS*, 224, 12
 Crossfield, I. J. M., Ciardi, D. R., Isaacson, H., et al. 2017, *AJ*, 153, 255
 Crossfield, I. J. M., & Kreidberg, L. 2017, *AJ*, 154, 261
 de Wit, J., Wakeford, H. R., Lewis, N. K., et al. 2018, *NatAs*, 2, 214
 Deming, D., Knutson, H., Kammer, J., et al. 2015, *ApJ*, 805, 132
 Deming, D., Wilkins, A., McCullough, P., et al. 2013, *ApJ*, 774, 95
 Evans, T. M., Sing, D. K., Kataria, T., et al. 2017, *Natur*, 548, 58
 Evans, T. M., Sing, D. K., Wakeford, H. R., et al. 2016, *ApJL*, 822, L4
 Fazio, G. G., Hora, J. L., Allen, L. E., et al. 2004, *ApJS*, 154, 10
 Feroz, F., & Hobson, M. P. 2008, *MNRAS*, 384, 449
 Feroz, F., Hobson, M. P., & Bridges, M. 2009, *MNRAS*, 398, 1601
 Feroz, F., Hobson, M. P., Cameron, E., & Pettitt, A. N. 2013, arXiv:1306.2144
 Fortney, J. J., Lodders, K., Marley, M. S., & Freedman, R. S. 2008, *ApJ*, 678, 1419
 Fortney, J. J., Mordasini, C., Nettelmann, N., et al. 2013, *ApJ*, 775, 80
 Fortney, J. J., & Nettelmann, N. 2010, *SSRv*, 152, 423
 Fraine, J., Deming, D., Benneke, B., et al. 2014, *Natur*, 513, 526
 Freedman, R. S., Lustig-Yaeger, J., Fortney, J. J., et al. 2014, *ApJS*, 214, 25
 Freedman, R. S., Marley, M. S., & Lodders, K. 2008, *ApJS*, 174, 504
 Gao, P., & Benneke, B. 2018, *ApJ*, 863, 165
 Greene, T. P., Line, M. R., Montero, C., et al. 2016, *ApJ*, 817, 17
 Guo, X., Crossfield, I. J. M., Dragomir, D., et al. 2020, *AJ*, 159, 239
 He, C., Hörst, S. M., Lewis, N. K., et al. 2018, *AJ*, 156, 38
 Helled, R., Nettelmann, N., & Guillot, T. 2020, *SSRv*, 216, 38
 Hess, M., Koepke, P., & Schult, I. 1998, *BAMS*, 79, 831
 Horne, K. 1986, *PASP*, 98, 609
 Hörst, S. M., He, C., Lewis, N. K., et al. 2018, *NatAs*, 2, 303
 Houk, N., & Swift, C. 1999, Michigan Spectral Survey, Vol. 5 (Ann Arbor, MI: Univ. Michigan)
 Hubbard, W. B., Nellis, W. J., Mitchell, A. C., et al. 1991, *Sci*, 253, 648
 Hunter, J. D. 2007, *CSE*, 9, 90
 Kass, R. E., & Raftery, A. E. 1995, *JASA*, 90, 773
 Kawashima, Y., Hu, R., & Ikoma, M. 2019, *ApJL*, 876, L5
 Kawashima, Y., & Ikoma, M. 2018, *ApJ*, 853, 7
 Kawashima, Y., & Ikoma, M. 2019, *ApJ*, 877, 109
 Kempton, E. M. R., Bean, J. L., Louie, D. R., et al. 2018, *PASP*, 130, 114401
 Khare, B. N., Sagan, C., Arakawa, E. T., et al. 1984, *Icar*, 60, 127
 Knutson, H. A., Benneke, B., Deming, D., & Homeier, D. 2014, *Natur*, 505, 66
 Kosiarek, M. R., Berardo, D. A., Crossfield, I. J. M., et al. 2021, *AJ*, 161, 47

- Kreidberg, L. 2015, *PASP*, **127**, 1161
- Kreidberg, L., Bean, J. L., Désert, J.-M., et al. 2014, *Natur*, **505**, 69
- Kreidberg, L., Line, M. R., Thorngren, D., Morley, C. V., & Stevenson, K. B. 2018a, *ApJL*, **858**, L6
- Kreidberg, L., Line, M. R., Parmentier, V., et al. 2018b, *AJ*, **156**, 17
- Libby-Roberts, J. E., Berta-Thompson, Z. K., Désert, J.-M., et al. 2020, *AJ*, **159**, 57
- Lodders, K. 2003, *ApJ*, **591**, 1220
- Lopez, E. D., & Fortney, J. J. 2013, *ApJ*, **776**, 2
- Madhusudhan, N., Amin, M. A., & Kennedy, G. M. 2014, *ApJL*, **794**, L12
- Madhusudhan, N., Nixon, M. C., Welbanks, L., Piette, A. A. A., & Booth, R. A. 2020, *ApJL*, **891**, L7
- Mansfield, M., Bean, J. L., Oklopčić, A., et al. 2018, *ApJL*, **868**, L34
- Marley, M. S., & McKay, C. P. 1999, *Icar*, **138**, 268
- Marley, Mark S., Saumon, Didier, Visscher, Channon, et al. 2021, *ApJ*, **920**, 85
- McKay, C. P., Pollack, J. B., & Courtin, R. 1989, *Icar*, **80**, 23
- Mollière, P., Wardenier, J. P., van Boekel, R., et al. 2019, *A&A*, **627**, A67
- Morley, C. V., Fortney, J. J., Kempton, E. M.-R., et al. 2013, *ApJ*, **775**, 33
- Morley, C. V., Fortney, J. J., Marley, M. S., et al. 2012, *ApJ*, **756**, 172
- Morley, C. V., Fortney, J. J., Marley, M. S., et al. 2015, *ApJ*, **815**, 110
- Morley, C. V., Knutson, H., Line, M., et al. 2017, *AJ*, **153**, 86
- Moses, J. I., Madhusudhan, N., Visscher, C., & Freedman, R. S. 2013, *ApJ*, **763**, 25
- Nettelmann, N., Helled, R., Fortney, J. J., & Redmer, R. 2013, *P&SS*, **77**, 143
- Ohno, K., Okuzumi, S., & Tazaki, R. 2020, *ApJ*, **891**, 131
- Owen, J. E., & Wu, Y. 2013, *ApJ*, **775**, 105
- Parmentier, V., & Guillot, T. 2014, *A&A*, **562**, A133
- Parmentier, V., Guillot, T., Fortney, J. J., & Marley, M. S. 2015, *A&A*, **574**, A35
- Pont, F., Sing, D. K., Gibson, N. P., et al. 2013, *MNRAS*, **432**, 2917
- Rackham, B. V., Apai, D., & Giampapa, M. S. 2018, *ApJ*, **853**, 122
- Rackham, B. V., Apai, D., & Giampapa, M. S. 2019, *AJ*, **157**, 96
- Rodrigo, C., & Solano, E. 2013, Filter Profile Service Access Protocol, v1.0, IVOA
- Rodrigo, C., Solano, E., & Bayo, A. 2012, SVO Filter Profile Service, v1.0, IVOA
- Rodriguez, J. E., Zhou, G., Vanderburg, A., et al. 2017, *AJ*, **153**, 256
- Rogers, L. A., & Seager, S. 2010, *ApJ*, **716**, 1208
- Rothman, L. S., Rinsland, C. P., Goldman, A., et al. 1998, *JQSRT*, **60**, 665
- Saumon, D., & Marley, M. S. 2008, *ApJ*, **689**, 1327
- Segura, A., Krelove, K., Kasting, J. F., et al. 2003, *AsBio*, **3**, 689
- Simon, A. A., Fletcher, L. N., Arridge, C., et al. 2020, *SSRv*, **216**, 17
- Skilling, J. 2004, in AIP Conf. Ser. 735, Bayesian Inference and Maximum Entropy Methods in Science and Engineering, ed. R. Fischer, R. Preuss, & U. V. Toussaint (Melville, NY: AIP), 395
- Spake, J. J., Sing, D. K., Evans, T. M., et al. 2018, *Natur*, **557**, 68
- Speagle, J. S. 2020, *MNRAS*, **493**, 3132
- Tennyson, J., Yurchenko, S. N., Al-Refaie, A. F., et al. 2016, *JMoSp*, **327**, 73
- Thorngren, D., & Fortney, J. J. 2019, *ApJL*, **874**, L31
- Thorngren, D. P., Fortney, J. J., Murray-Clay, R. A., & Lopez, E. D. 2016, *ApJ*, **831**, 64
- Valencia, D., Guillot, T., Parmentier, V., & Freedman, R. S. 2013, *ApJ*, **775**, 10
- van der Walt, S., Colbert, S. C., & Varoquaux, G. 2011, *CSE*, **13**, 22
- Virtanen, P., Gommers, R., Oliphant, T. E., et al. 2020, *NatMe*, **17**, 261
- Wakeford, H. R., Sing, D. K., Kataria, T., et al. 2017, *Sci*, **356**, 628
- Werner, M. W., Roellig, T. L., Low, F. J., et al. 2004, *ApJS*, **154**, 1
- Wolfgang, A., & Lopez, E. 2015, *ApJ*, **806**, 183
- Wong, I., Benneke, B., Gao, P., et al. 2020, *AJ*, **159**, 234
- Zhou, G., Rodriguez, J. E., Vanderburg, A., et al. 2018, *AJ*, **156**, 93
- Zhou, Y., Apai, D., Lew, B. W. P., & Schneider, G. 2017, *AJ*, **153**, 243